Mon. Not. R. Astron. Soc. **000**, 1–9 (2002) Printed 25 March 2014 (MN LATEX style file v2.2)

CIR Modulation of the X-ray Flux from the O7.5 III(n)((f)) Star ξ Persei*?

D. Massa[1]†, L. Oskinova[2], A. W. Fullerton[3], R. K. Prinja[4], D. A. Bohlender[5], N. D. Morrison[6], M. Blake[7] and W. Pych[8]

[1] *Space Science Institute, 4750 Walnut St, Suite 205, Boulder, CO 80301, USA*
[2] *Institute for Physics and Astronomy, University Potsdam, 14476 Potsdam, Germany*
[3] *Space Telescope Science Institute, 3700 San Martin Dr., Baltimore, MD 21218, USA*
[4] *Dept. of Physics & Astronomy, University College London, Gower St., London, England WC1E 6BT*
[5] *National Research Council of Canada, 5071 W. Saanich Rd., Victoria, BC V9E 2E7, Canada*
[6] *Ritter Observatory, Dept. of Physics & Astronomy, The University of Toledo, Toledo, OH 43606-3390, USA*
[7] *UNA Box 5263 University of North Alabama Florence, Alabama 35632*
[8] *Nicolaus Copernicus Astronomical Centre Polish Academy of Sciences ul. Bartycka 18 00-716 Warszawa Poland*

Accepted 1988 December 15. Received 1988 December 14; in original form 1988 October 11

ABSTRACT

We analyze a 162 ks HETG *Chandra* observation of the O7.5 III(n)((f)) star ξ Per, together with contemporaneous Hα observations. The X-ray spectrum of this star is similar to other single O stars, and not pathological in any way. Its UV wind lines are known to display cyclical time variability, with a period of 2.086 days, which is thought to be associated with co-rotating interaction regions (CIRs). We examine the *Chandra* and Hα data for variability on this time scale. We find that the X-rays vary by $\sim 15\%$ over the course of the observations and that this variability is out of phase with variable absorption on the blue wing of the Hα profiles (assumed to be a surrogate for the UV absorption associated with CIRs). While not conclusive, both sets of data are consistent with models where the CIRs are either a source of X-rays or modulate them.

Key words: stars: individual (HD 24912) — stars: early-type — stars: winds, outflows — X-rays: stars

1 INTRODUCTION

X-ray emission is ubiquitous in the O stars and taken as an indication of dynamic instabilities in their winds (Lucy & White 1980; Lucy 1982; Owocki et al. 1988; Feldmeier et al. 1997). These 1-D hydrodynamical models predict a plasma with temperature ~ 1 –10 MK, which is permeated with cool wind clumps. The models also predict very strong stochastic X-ray variability, on time scales of hours. However, it has been clear since early X-ray observations, that stochastic variability on such short time scales is very small, less than about 1%. To explain this, Cassinelli (1983) suggested that the winds contain thousands of shocks, and Feldmeier et al. (1997) speculated that models with full 2-D hydrodynamics would reduce the predicted level of stochastic X-ray variability. In the most extensive analysis to date, Nazé et al. (2013) examined high quality *XMM-Newton* observations of the early O supergiant ζ Pup. They used an *ad hoc* 2-D wind model and found that the lack of stochastic X-ray variability on short time scales required a highly fragmented wind with a huge number of small clumps. In this picture, a stellar wind consists of a large population of cool clumps, which contain the bulk of the stellar wind matter seen at UV, optical, IR and radio wavelengths, and a tenuous hot interclump medium responsible for the X-rays. Further evidence for small scale clumping has come from the analysis of optical and UV wind lines. Hillier (1991) found that it was necessary to introduce clumping to explain the shapes of electron scattering emission line wings in Wolf-Rayet (WR) stars. Given the 1-dimensional nature of his model, this would imply the presence of either concentric shells or random structures whose size and separation are much smaller than the Sobolev length, so that the angle integrations are meaningful. Stochastic variable features in the He II λ4686 Å emission line in ζ Pup were found by Eversberg et al. (1998), and explained as excess emission from the wind clumps.

* Based on data obtained with the Chandra X-Ray Observatory.
† E-mail: dmassa@spacescience.org

Markova et al. (2005) investigated Hα line-profile variability in a large sample of O-type supergiants, and concluded that the observed variability can be explained by a wind model consisting of coherent or broken shells. Lépine & Moffat (2008) presented direct spectroscopic evidence of clumping in O and WR star winds.

Besides this small scale clumping, a different, perhaps related, aspect of O star winds is that all of them which have been observed over time scales of a day or more demonstrate temporally coherent UV wind line variability (e.g., Massa et al. 1995; Kaper et al. 1996, 1999). This phenomenon suggests the presence of large structures in their winds which **may** originate from large regions on the surface of the star. These results led Cranmer & Owocki (1996) to model wind variability by large spiral structures known as Co-rotating Interaction Regions (CIRs, Mullan 1986). These structures originate from large regions of enhanced wind flux on the surface of the star, although the exact cause of the enhanced wind remains unexplained. Hamann et al. (2001) showed that the observed UV line variability cannot be simply explained as a consequence of rotation in the framework of the CIR model, and a more complex interplay between rotation and radial velocity is taking place. Further, Prinja & Massa (2010) analyzed the doublet ratios of wind lines of a large number of B supergiants. Their results demonstrated that the spectral signature of large, optically thick wind structures which cover only a portion of the line of sight to the stellar disk (most likely CIRs) is common in the B supergiants.

The interplay between CIRs and small scale clumping is largely unexplored. A crude analysis by Owocki (1999) suggested an intricate interaction between the two. Lobel & Blomme (2008) considered 3-D hydrodynamic models of CIRs. While their models could reproduce the detailed time evolution of UV spectral features in a B-type supergiant, they expressed concern that too much small scale clumping could destroy the CIRs. Whatever the mechanism of X-ray production, the presence of large scale structures in stellar winds should leave a footprint on the X-ray emission. In particular, X-ray variability on a time scale compatible with the stellar rotation period should be present, and this X-ray variability should correlate with UV wind line variability. However, there are considerable observational obstacles to establishing a link between X-ray and UV wind line variability for single, normal O stars. First, the CIRs are thought to be confined to the equatorial plane. Consequently, variability may not be seen unless our line of sight to the star is relatively close to equator-on. Second, the stellar rotation period for most O stars is several days. This is considerably longer than the typical X-ray observation, so variability could easily be missed. Third, there are only a few stars which have been observed in the UV over long enough intervals for good wind line periods to be identified, and such a period is needed to claim a definite connection between X-ray and UV wind line variability. Fourth, binary stars with colliding stellar winds must be excluded from any investigation of the connection between X-rays and large scale wind structure.

Despite these hurdles, observational evidence supporting a link between CIRs and X-ray emission from stellar winds is mounting. Recently, X-ray variability of $\sim$ 20% and on the time scale of recurrent DACs was detected in the WR star EZ CMa, and explained in the framework of the CIR model (Oskinova et al. 2012; Ignace et al. 2013). More relevant to the current paper, is the work on O stars by Berghöfer et al. (1996), Oskinova et al. (2001) and Nazé et al. (2013). Berghöfer et al. (1996) found a marginal detection of a periodic X-ray variability in ζ Pup, which was not confirmed by Oskinova et al. (2001) or Kahn et al. (2001) and not in agreement with DAC period determined by Howarth et al. (1995). Nazé et al. (2013) analyzed a series of X-ray observations of ζ Pup which span 10 years. They detected a slow modulation of the X-ray flux with a relative amplitude up to 15% over 16 hours in the 0.3-4.0 keV band. They propose that these modulations can be attributed to CIRs. The most compelling evidence to date was given by the Oskinova et al. (2001) analysis of the rapidly rotating O dwarf ζ Oph. It is the only single O star that has been observed continuously in X-rays over a full rotational period. These observations showed that the X-ray variability occurred on a time scale similar to the UV wind line variability, but they were not long enough to show that the pattern repeated on the rotation time scale. Unfortunately, there were no simultaneous observations of the wind activity that could be used to determine the phase relation between the X-ray and wind activity. Such a relationship could provide valuable clues about the geometric relationship between the X-ray emitting plasma and the CIRs.

In this paper we present X-ray observations covering nearly half of a rotation period of the O7 III(n)((f)) star ξ Per, supplemented by optical Hα observations which bracket the X-ray observations. ξ Per is an ideal candidate for attempting to make a connection between UV wind line and X-ray variability. First of all, ξ Per appears to be a perfectly normal O7 giant (see, Walborn 1973; Walborn et al. 1985, for descriptions of its optical and UV spectra, respectively). Its only distinguishing feature is that it has a somewhat high (but not abnormal) rotational velocity of $v \sin i = 204$ km s^{-1} (Penny 1996). Because of its moderate $v \sin i$, its expected rotation period is short enough to be captured by a time series of manageable duration. This was done in a detailed study of its UV and optical line variability by de Jong et al. (2001). They demonstrated the presence of a well characterized, distinctive 2.086 day period in the UV wind line variability. This turns out to be roughly half of the expected rotation period if the star is viewed nearly equator-on (see their Figure 4). Further, they were able to model the variability by two sets of two armed CIRs (see, their Figure 17), with one set of arms dominating the variability. They were also able to establish a relationship between the appearance of the discrete absorption components (DACs) associated with the CIRs and variations in the blue wing of Hα, which enable us to use Hα variability as a surrogate for DAC activity. These properties of ξ Per, together with its relative brightness at X-ray wavelengths, make it an ideal candidate to determine whether the CIRs that are thought to modulate the UV wind lines in this star (and possibly all luminous OB stars with massive winds) might modulate its X-ray flux as well. To pursue this conjecture, we obtained a 162 ks (0.45 rotation periods and 0.90 periods of the strong CIR activity) *Chandra* observation of ξ Per.

The X-ray and optical observations are described in §2, anlyzed for variability in §3 and discussed in §4.

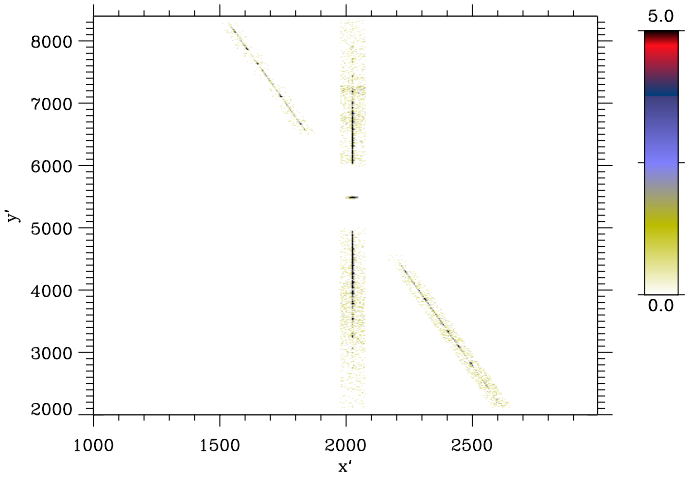

Figure 1. Partial image of the *Chandra* data of ξ Per in a coordinate frame rotated so that the MEG spectrum is a vertical stripe. This image contains only events filtered as described in the text. The spot near the center of the image is the zeroth order image and the faint diagonal stripe is the HEG spectrum.

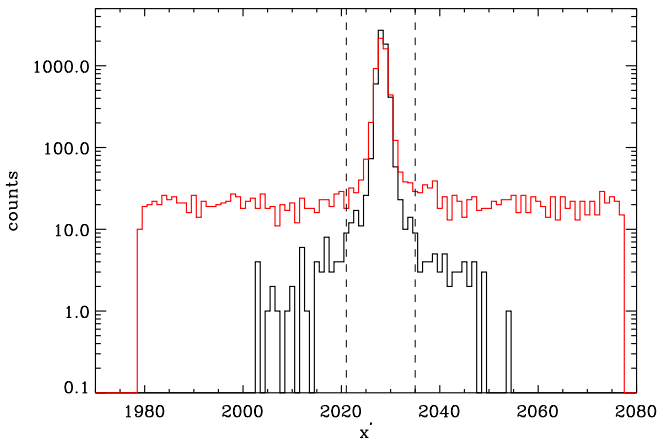

Figure 2. Cross dispersion profiles for the $M = \pm 1$ MEG (red) spectra and $M = 0$ (black) image. Each profile is the total number of counts for the order collapsed along the y' axis shown in Figure 1. The filtering of the data is described in the text.

2 THE OBSERVATIONS AND DATA REDUCTION

2.1 X-ray Data

Although a continuous observation of 2.1 d is required to be certain that the full range of variability is observed, as one arm of the CIR pattern traverses our line of sight, the maximum visibility of ξ Per to *Chandra* was ~ 162 ks (1.9 d), or roughly 90% of the UV wind line modulation period. The observations were obtained with *Chandra*'s transmission High Energy Transmission Grating Spectrometer (HETGS) and began on 2004 March 22 (MJD = 53086.0904).

The high energy transmission grating, HETG, consists of two sets of gratings; the Medium Energy Grating (MEG) and the High Energy Grating (HEG) (*Chandra* X-ray Center 2012). The events were recorded on the ACIS-S chips and consist of a $\pm$ first order dispersed spectrum for both the MEG and HEG and a directly transmitted, zeroth order, image. Some spectral information can be extracted from the zeroth order image through the energy determined for the individual events. All of the data were processed with version 3.3 of the *Chandra* Interactive Analysis of Observations (CIAO) software package. The newly reduced data can be found in the "The *Chandra* Grating-Data Archive and Catalog (TGCat)" (Huenemoerder et al. 2011). See the CIAO documents for further information[1].

Pile-up (the arrival of two photons near the same location between CCD reads) was not a major issue for the observations. The strongest lines in the MEG spectra only had count rates of $\lesssim 1.0 \times 10^{-3}$ counts s^{-1} and the count rate of the zeroth order image was $\lesssim 0.04$ counts s^{-1}. In the first case, pile-up is completely negligible, and in the latter it never exceeds 5%. Further, pile up will only mute the amplitude of variability and not make a constant source appear variable.

[1] http://cxc.harvard.edu/ciao/intro/

We now describe how we filtered the initial data to maximize the contribution from the source and minimize background effects. We utilize the *Chandra* primary time tag photon list for our analysis. Specifically, we use the following tags attached to each event: x and y, the sky coordinates; *energy*, the event energy estimated from the number of CCD counts it created; *grade*, the shape descriptor of the CCD count distribution of the event; *time*, the time at which the event was read; *tg_m*, the likely grating order, M, associated with an event; *tg_lam*, the wavelength for the $M = \pm 1$ events based on their location relative to the dispersion, and; *tg_part*, the probable association of a photon with either the HEG or MEG spectrum of the zeroth order image based on its location. See, the CIAO web site for further information.

To simplify matters, we begin by "rotating" the x and y sky coordinates by $\theta = -29.31^\circ$, to produce a primed coordinate system in which the first order MEG spectra are aligned with the y'-axis. Figure 1 shows a portion of the detector in the rotated frame. The events in this image have been filtered as follows: $|M| \leqslant 2$, ASCA grades of 0, 2, 3, 4, 5 or 6 (as done in normal processing), and $0.4769 \leqslant energy \leqslant 2.0664$ keV, which corresponds to the wavelength range of interest, $6 \leqslant \lambda \leqslant 26$ Å. The $M = 0$ image appears as a spot near the center of the figure, and the MEG $M = \pm 1$ spectra are the vertical strips which lie on either side of it. The faint diagonal stripes are the HEG spectra, which are not considered further, since they contain very few counts.

We note two important properties of Figure 1. First, the zeroth order image is localized and resides on a single CCD. Second, in spite of filtering, there are considerable extraneous events in the cross-dispersion direction, well away from the center of the MEG $M = \pm 1$ spectra. To emphasize this, we filtered the events list further to produce cross-dispersion profiles. Figure 2 shows the cross dispersion profiles for the MEG $M = \pm 1$ events collapsed along the y' axis, compared to all of the $M = 0$ events, similarly collapsed. The first order events were restricted further to include only counts with *tg_part* = 2 (which eliminates HEG data) and wavelength tags in the range $6 \leqslant \lambda \leqslant 26$Å. This last restriction

differs from the energy filtering since it also includes location on the detector.

Because the events on the wings of the first order cross-dispersion profile do not appear in the zeroth order image, they are not from the sky. This is further verified by examining their spectral signature, which turns out to be featureless – free of emission lines. Therefore, these counts will not carry the time dependence of the source and we should eliminate as many as possible. To do this, we restrict the first order events to those which lie in the range $2021 \leqslant x' \leqslant 2035$. There are 5782 counts in the refined region, compared to 7580 when all x' events are included – a reduction of 31%. Assuming that the source counts are all contained in the restricted area and that the background counts are uniformly distributed over the region $1979 \leqslant x' \leqslant 2077$ (see Figure 2) we can estimate the total number of background and source counts. Let N_s and N_b be the total number of source and background counts over the region from $1979 \leqslant x' \leqslant 2077$. Now let $N_1 = 7580$ be the observed counts over the larger region and $N_2 = 5782$ be the observed counts over the restricted region. Then, $N_1 = N_s + N_b$ and $N_2 = N_s + N_b \times (2035 - 2021)/(2077 - 1979)$. Solving these two equations gives $N_s = 5482$ and $N_b = 2098$. Thus, 28% of N_1 are background counts compared to only 5.2% of N_2. Consequently, although some background counts remain in N_2, their effect should not be too great. In contrast, the $M = 0$ image has 5915 counts and appears to contain far fewer background counts. Therefore, it was not filtered any further.

The filtered events from the zeroth order image and first order spectra were resampled into 2 hour time bins for better statistics. Figure 3 compares the two time series. In this figure, each series was normalized by its mean value for comparison purposes and the error bars are based on Poisson statistics from the number of counts in each bin. It is clear that both series display a general decreasing trend over the extent of the observation. Therefore, the two were added to arrive at the summed series shown in Figure 4, where each bin contains several hundred counts, making it reasonable to approximate the intrinsic Poisson statistics by Gaussian statistics.

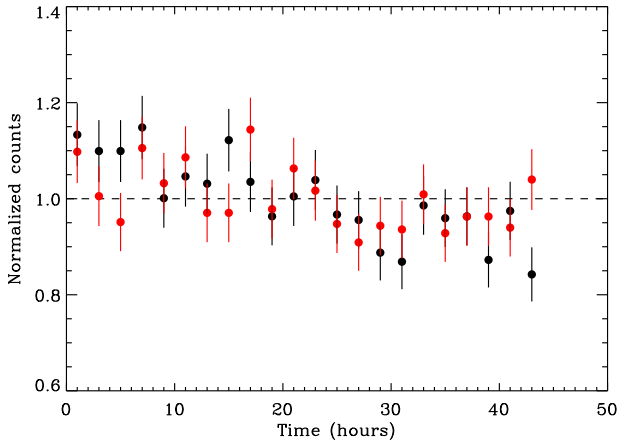

Figure 3. Total counts in the $M = \pm 1$ MEG spectra (red) and the $M = 0$ (black) image resampled into 2 hour bins and normalized by their mean counts. The error bars are based on the total number of counts contained in each time bin.

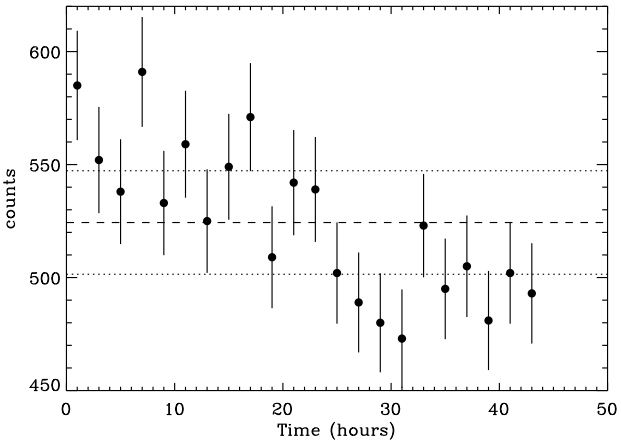

Figure 4. Total counts in the combined $M = \pm 1$ and $M = 0$ MEG spectra resampled into 2 hour bins.

2.2 Optical Data

While the period of DAC variability in ξ Per is reasonably well defined, it probably originates from surface features, and there is no reason to expect long term coherence. Consequently, to determine the phase relation between the X-ray and DAC variability at the time of the *Chandra* time series, we need observations which predict DAC occurrence and are obtained close to the time of the X-ray observations. To do this, we use the de Jong et al. (2001) result that variable absorption of the blue wing of Hα is essentially in phase with the DACs (see their Table 5). Consequently, Hα observations were obtained within $\sim \pm 7$ days of the *Chandra* data, in order to determine the relative phases of the X-rays and the DACs. Spectra were obtained at three North American sites: the David Dunlap Observatory (DDO); the Ritter Observatory (Ritter); and the Dominion Astrophysical Observatory (DAO).

Our optical observations bracket and overlap the X-ray observations. They begin 6.6 days prior to the *Chandra* observations and conclude 7.7 days after. They span a total of 16.1 days, roughly centered on the *Chandra* series. Since de Jong et al. (2001) have demonstrated that the CIR related spectral features remain well phased over the 9.4 day interval of their *IUE* time series, it seems reasonable to assume that they remain in phase over the time interval of our optical data, which is less than twice as long.

DDO Observations: One high-quality spectrum was obtained with the Cassegrain spectrograph of the DDO 1.88m telescope. The observation was made through a 242 μm slit with the 1800 lines/mm grating in first order. The detector was a Jobin-Yvon thinned, back-illuminated CCD with 2000×800 pixels. This configuration provided a linear reciprocal dispersion of 0.153 Å per 15 μm pixel. Bias frames, tungsten lamp flat field observations and Fe-Ar lamp wavelength observations were obtained immediately before and after the stellar observation.

Ritter Observations: Three spectra were obtained with

the Ritter 1.06 m telescope. These were obtained with the bench-mounted échelle spectrograph, coupled to the Cassegrain focus of the telescope by a 200 μm wide optical fiber. The detector was a front-illuminated EEV CCD with 1200×800 pixels, each of which is 22.5 μm square. At Hα (order 34), the spectrograph has resolving power of 2.6×10^4, and the entrance slit projects to ∼4.3 pixels. The observed positions of telluric water vapour lines were first used with the wavelengths given by Hinkle et al. (2000) to correct nonlinearities in the wavelength scale determined from the comparison arc. After telluric correction, the Ritter spectra were binned by a factor of 2 to improve the S/N.

DAO Observations: The DAO 1.22m McKellar telescope and coudé spectrograph were used in "robotic" mode to obtain seventeen spectra on 4 nights. The "9681M" configuration of the spectrograph was used with the SITe-4 CCD detector, which is a thinned, back-illuminated array of 4096 × 2048 pixels, each of which is 15 μm square. This configuration results in a spectrum with linear reciprocal dispersion of 0.073 Å/pixel. Additional observations of a tungsten continuum source and Th-Ar emission spectrum were obtained to provide flat field and wavelength calibrations, respectively.

Standard *IRAF*[2] routines were used to process the CCD frames obtained at all three observatories. Telluric line contamination was removed by using templates derived from contemporaneous spectra of the rapidly rotating B7 V α Leo.

The late March date of the *Chandra* observations had two consquences for the ground-based campaign. First, ξ Per could only be observed for $\lesssim$2 hours at the beginning of each night. Consequently, a significant phase range of the 2.086-day period could not be covered during a single night, and nearly the same phase was observed every second night. Second, the weather is not traditionally very good at any of the observatories in March. As a result, the phase coverage is fairly sparse.

Since the phase coverage on any given night was extremely limited, mean spectra were computed whenever possible in order to improve the signal-to-noise (S/N) ratio. The nightly mean spectra are illustrated in Figure 5. We define the "blue wing" equivalent width of Hα, W_B(Hα), as the integrated mean spectra between $(-500, -200)$ km s^{-1} of line center (measured in the stellar reference frame). The prescription of Vollmann & Eversberg (2006) was used to estimate uncertainties in W_B(Hα).

Table 1 summarizes the optical data. Successive columns record the heliocentric Julian Data (HJD) corresponding to the mid-point of the mean spectrum; the observatory; the number of spectra averaged; the exposure time per spectrum in seconds; the S/N per pixel in the continuum of the mean spectrum; and W_B(Hα) in Å.

3 ANALYSIS

The mean HETGs spectrum of ξ Per was already presented by Oskinova, et al. (2006) and Walborn et al. (2009). The X-ray spectrum is similar to other single O-type stars whose X-ray line profiles can be described in the context of a clumped wind model with the X-ray emission originating relatively close to the stellar photosphere. Therefore, this work concentrates on the time variability.

If we simply take the standard deviation of the time series shown in Figure 4, we find that the probability that the scatter about the mean exceeds the observed value is 15%. Based on this, one might conclude that the evidence for variability is not very strong. However, this statistic does not consider the distinct temporal ordering of the deviations. The object of this section is to analyze the observed trend. We first assess the time variability by subjecting the un-binned data to the Kolmogorov-Smirnov test. Next, we examine the form of the autocorrelation function (e.g.,

[2] *IRAF* is distributed by the National Optical Astronomy Observatories, which are operated by the Association of Universities for Research in Astronomy, Inc., under cooperative agreement with the National Science Foundation.

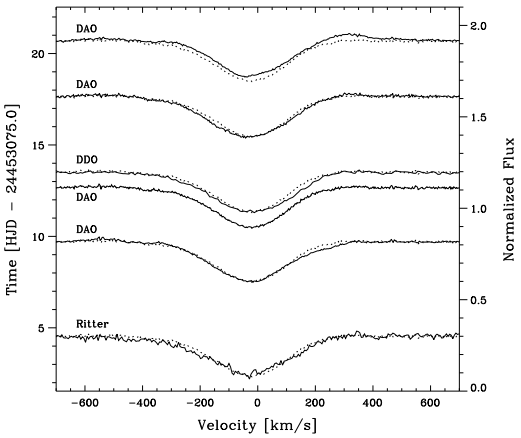

Figure 5. Nightly mean Hα spectra obtained contemporaneously with the *Chandra* X-ray observations. The abscissa denotes velocity in the frame of the star, for which a systemic velocity of 59.3 km s^{-1} has been adopted. Spectra are displaced vertically in proportion to the time difference between them, as indicated by the left-hand scale. The right-hand scale indicates normalized flux. To highlight changes, the mean DAO spectrum from 2004-03-23 is overplotted as a dotted line. Two Ritter spectra have not been plotted in order to avoid confusion with the other observations obtained on the same nights.

Table 1. Journal of Ground-Based Observations

HJD [a]	Obs.	N [b]	t_{exp} [s]	S/N [c]	W_B(Hα) [Å] [d]
53079.5386	Ritter	1	1987	112	0.25 ± 0.08
53084.7081	DAO	4	1200	397	0.13 ± 0.02
53087.5534	Ritter	1	3600	187	0.17 ± 0.05
53087.6730	DAO	3	1200	264	0.15 ± 0.04
53088.5196	DDO	1	212	211	0.20 ± 0.04
53088.5383	Ritter	1	3600	89	0.18 ± 0.10
53092.6395	DAO	1	1200	238	0.17 ± 0.04
53095.6826	DAO	7	1200	385	0.06 ± 0.02

[a] HJD − 2,400,000.0 at the mid-point of the mean spectrum.
[b] Number of spectra.
[c] S/N per pixel in the continuum of the mean spectrum.
[d] Measured between $(-500, -200)$ km s^{-1}.

Chatfield 2004) of the binned data. We then apply three different models for the time dependence. Next, we examine a hardness ratio of the data for variability. Finally, we examine the variability of the Hα spectra.

Unlike a simple χ^2 statistic, the Kolmogorov-Smirnov test accounts for the distribution of the variance in time. We applied the Kolmogorov-Smirnov test to compare the unbinned zeroth and first order events, subject to the final screening outlined in the previous section, to a uniform, non-variable, sequence. This test resulted in probabilities of 0.9984 and 0.9233, respectively, that the data were time variable. The difference probably results because the first order spectra contain more background contamination. The same test was applied to the combination of the two data sets and gave a probability of 0.9997 that it is variable. These results leave little doubt about the reality of the temporal variability.

To examine the time dependence more closely, we present the autocorrelation function of the binned time series in Figure 6. The dashed lines are $\pm 1/\sqrt{22}$, which are the $\pm 2\sigma$ limits for the expected values of the elements of a random sequence with 22 samples (Chatfield 2004). The fact that the first 3 autocorrelation coefficients exceed this value is also strong evidence that the series is time variable. Further, the shape of the autocorrelation function bares no resemblance to one expected from a random sequence. Instead, it is more indicative of a portion of a periodic signal with its broad, negative minimum near 25 hours (roughly half of the period), in agreement with expectations.

We next modeled the binned series shown in Figure 4 with three heuristic models:

(i) A linear model, which measures the overall trend in the data

$$\text{counts} = a_1 t + a_2 \ . \tag{1}$$

(ii) A trigonometric model, to search for evidence of repeatability

$$\text{counts} = a_1 \cos\left(\frac{t - a_2}{2\pi P}\right) + a_3 \ , \tag{2}$$

where P is fixed at 2.086d (de Jong et al. 2001).

(iii) An exponential decay model, to characterize the recovery from an episodic event

$$\text{counts} = a_1 e^{-t/a_2} + a_3 \ . \tag{3}$$

The results of this exercise are shown in Figure 7 and are summarized in Table 2. The top panel shows the linear fit and the bottom panel the cosine fit, replicated to demonstrate its consistency with a periodic function. We do not show the exponential fit since it is indistinguishable from the linear fit. Table 2 lists the fit parameters. There are two rows for each fit. The first row gives the name of the fitting function, the free parameters and the probability that the observed reduced χ^2 exceeds the value expected if the assumed functional form were exact. The second row gives the mono-variate uncertainties of the fit parameters.

The reduced χ^2 statistic indicates that the cosine function provides the best fit, but that it is not significantly better than the linear or exponential functions. The coefficient

Table 2. Fit Parameters

Function	a_1	a_2	a_3	Probability
linear	569.2	−2.07	–	0.59
	±10.0	±0.39	–	
cosine	35.8	7.9	520.8	0.62
	±6.5	±1.7	±5.0	
exponential	573.0	251.0	−2.0	0.53
	±3281	±1585	±3387	
Hα cosine	0.082	25.1	0.150	0.45
	±0.022	±1.6	±0.014	

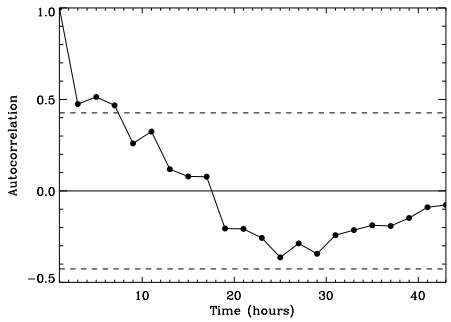

Figure 6. Autocorrelation function of the time series shown in Figure 4.

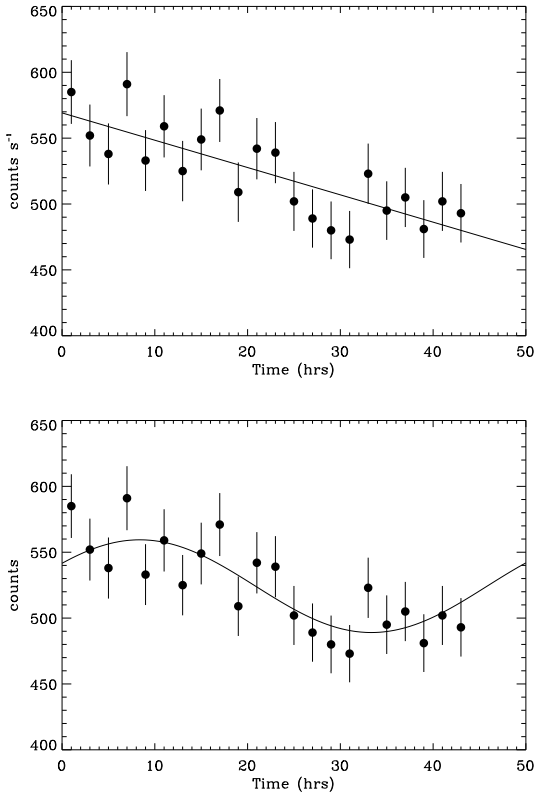

Figure 7. Fits of the total counts shown in Figure 4 to a linear function (top) and a trigonometric function (bottom). The fit parameters are given in Table 2.

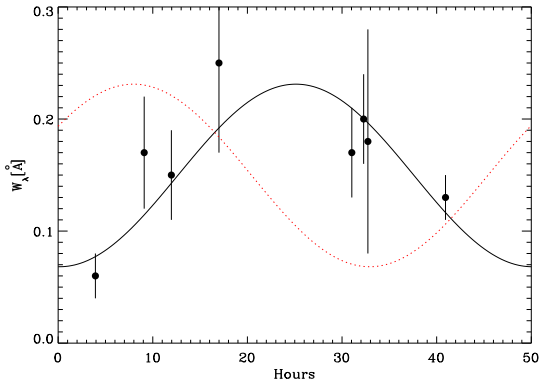

Figure 8. The strength of Hα blue-wing absorption fit by the cosine function given by eq. 2. The fit parameters are listed in Table 2. The red curve is the same fit, except with the X-ray value for the phase, a_2. The optical data have been wrapped on the 2.086-day period and phased to the beginning of the X-ray time series.

errors are extremely large for the exponential because they are strongly correlated, i.e., the coefficients can be changed together by large, but related, amounts and still produce a good fit.

Finally, we examined the time dependence of the hardness ratio. This was done by dividing the combined MEG $M = \pm 1$ and $M = 0$ spectrum into two bands: a "soft" band (events with $0.477 \leqslant h\nu < 0.954$ keV), and; a "hard" band (events with $0.954 \leqslant h\nu < 2.066$ keV). This division gives comparable counts in each band. We then examined the time dependence of their ratio in 2 hour bins for variability. The errors for the ratios were calculated using standard propagation of errors. In this case, no significant evidence for variability was found. For example, dividing the high energy bin by the lower energy bin gives 0.790 ± 0.026 over the first half of the observation and 0.811 ± 0.027 over the second half. Because the bulk wind opacity scales as $\sim \lambda^{-3}$, if an overall variability $\sim 15\%$ is due to variable absorption (as might be caused by periodic occultation by the spiral CIR pattern), one might expect an even larger variation at shorter wavelengths. However, this is not observed. One possible explanation for the absence of wavelength dependence of the variability is optically thick structures which occult different fractions of the source of the X-rays. If this is the case, the X-ray variability and its lack of wavelength dependence may provide powerful constraints on the geometry of CIRs and the source of the X-rays.

We now turn to the Hα data. Figure 8 shows the W_B(Hα) data fit by the same cosine function used for the X-rays along with the cosine function phased to the X-rays. The fit parameters are listed in Table 2. Although the data are sparse and the error bars large, formally, the fit is quite good. The Hα and the X-rays are 17.2 hours, or 124°, out of phase. This means that when the Hα absorption is strongest, the X-ray emission is nearly at its weakest.

The major results of this section are that the X-ray spectrum of ξ Per is variable at the level of $\sim 15\%$ (determined from the cosine fit parameters), that the variability is consistent with modulation by the 2.086 day period associated with the CIRs, that no variation in the hardness of the spectrum could be detected, suggesting that the variability is due to partial obscuration by optically thick structures and that the magnitude of W_B(Hα) is distinctly out of phase with the intensity of the X-rays.

4 DISCUSSION

There are basically two ways to generate X-ray variability. One is *via* an impulsive event, and the other is by occulting the source with absorbing gas or the stellar disk, as in the case of ζ Oph (Oskinova et al. 2001). However, if the variability were due to an impulsive, flare-like event, it must have occurred long before the observations (since the form of the variability is nearly linear, indicative of an exponential tail). This implies that the event would have been quite strong. Another possibility would be a flare on an unseen pre-main sequence companion. However, the X-ray luminosity of ξ Per is $\simeq 1.2 \times 10^{32}$ erg sec^{-1} (Oskinova, et al. 2006), while the X-ray luminosities of PMS stars are typically a factor of 10 smaller (see, Preibisch & Feigelson 2005). Further, the observed spectral change is grey and soft, very uncharacteristic for flare spectra (e.g. Guedel & Nazé 2009). While not impossible, either scenario seems unlikely, especially since the form of the variability and its autocorrelation function are consistent with cyclical behavior. As a result, we favor the explanation that the X-rays vary because of obscuration by intervening material.

In addition to ξ Per, X-ray variability has been observed in two other single, non-magnetic O stars: ζ Pup (O4 If(n), Nazé et al. 2013), and ζ Oph (O9.5 Vnn, Oskinova et al. 2001). Both vary on time scales which may be related to their stellar rotation periods. An analysis of several years of X-ray data for ζ Pup showed evidence for variability on a time scale similar to its DACs, but no single time series encompassed a rotation period. The best evidence for the interaction between CIRs and X-rays to date is the ζ Oph data set. It was observed for $\sim$ 1.2 days and its X-ray flux was found to vary by about 20%. Further, this variation appeared to repeat with a period of about 0.77 days, roughly half of the stellar rotation period and similar to a period previously determined from its UV wind lines (0.875 ± 0.167 days) by Howarth et al. (1993). However, no information relating the phases of the X-rays and the DACs was available, so it was impossible to constrain the geometry of the CIRs and X-rays.

In this paper, we have presented three observational results which help constrain the relation of the CIRs and X-rays. These are: X-ray variability, consistent with the period observed in the DACs; a constant hardness ratio for the X-rays, suggesting that the source of the X-rays becomes partial obscured by optically thick structures along the line of sight, and; a phase lag of 124° between the maximum absorption on the blue wing of Hα and the maximum strength of the X-rays.

To interpret our limited set of observations (covering roughly half of a rotation period) in terms of the geometry of CIRs requires some constraints. We follow de Jong et al. (2001) and adopt the following 3 assumptions:

(i) **The wind of ξ Per contains two pairs of spiral arms, with one arm in each pair being much stronger**

than the other. We concentrate on the two major arms, which are equally spaced.

(ii) The wind structures follow streak lines whose shapes are defined by the stellar rotational velocity, wind velocity law and terminal velocity. We adopt a rotational velocity equal to the observed $v \sin i = 205$ km s^{-1}, a velocity law of the form $v = v_\infty[1 - a/(r/R_\star)]$, where $v_\infty = 2420$ km s^{-1} and $1 - a = v(r = 1) = 0.01 v_\infty$.

(iii) The Hα emission originates near the base of the wind and is associated with the spiral structures. Since increased emission reduces W_B(Hα), the Hα emission and X-ray variability are nearly in phase.

In addition, we note that the grey nature of the variability suggests that the X-ray variations are due to occultation of the X-ray source by either the stellar disk or wind structures that are optically very thick to X-rays.

Thus, we seek configurations where the X-ray emission and Hα emission are roughly in phase. However, even with these restrictions, there is still considerable latitude in how the geometry can be arranged. We consider two possibilities, but others may be possible.

The right panel of Figure 9 shows the first configuration. It places the X-ray emission along the interacting edge of the spirals. This might be the case if some or most of the X-rays originate at the fast wind–slow wind interface, which creates the CIRs. Further, because the velocity differential between the fast and slow winds (and, presumably the potential to produce X-rays) is expected to drop with distance from the star, one expects most of the X-rays to originate within $\sim 5R_\star$. Thus, viewing the Figure from the right, we see that the Hα and X-ray emitting regions are at or near maximum. Then, as the configuration rotates counter-clockwise, our view would be from below. In this case, one lobe of the Hα emission and much of the X-ray emission near the star are occulted by the stellar disk, producing a minimum in both. Finally, as the system rotates further and our view is from the left, and we have returned to a maximum once again.

For this configuration to explain the observations, the arms must represent a relatively low density contrast in the wind since we do not observe spectral changes in the X-ray spectrum indicative of absorption. This is in accordance with typical CIR models, where UV DAC formation is attributed mostly to a velocity plateau. However, in contrast to the classic line driven instability (LDI) model (which predicts that the X-ray source should be distributed relatively uniformly throughout the wind) the observed variability implies that the CIRs must account for a large fraction of the X-rays.

The left panel of Figure 9 depicts a second possible configuration. It consists of a spherically symmetric X-ray emitting region which is heavily weighted toward the inner wind (in accordance with the LDI model) and two spiral arms. As before, the Hα emission originates near the base of the spiral arms. To obtain the X-ray variability, we must assume that the spiral arms are optically very thick, and that their line of sight optical depth decreases with distance from the star. The latter assumption corresponds to the spiral structures expanding with a constant solid angle, causing their line of sight column density to decrease as $(r/R_\star)^2$ near the star. As a result, sight lines toward the inner wind are strongly

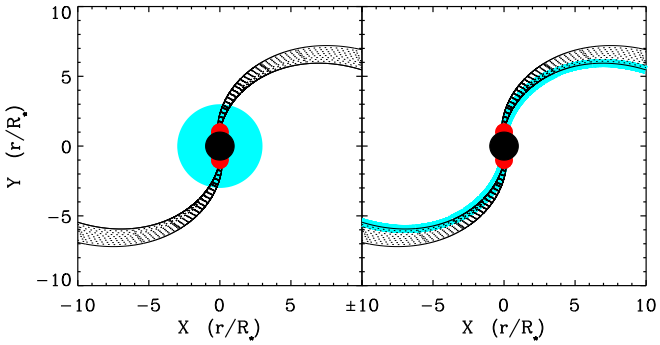

Figure 9. Cartoons of two different configurations of the Hα and X-ray emitting regions in a wind containing two spiral structures in the shape of streak lines. In each case, the Hα emitting region is depicted by two red dots, and the X-ray emitting region by an aqua region. The coordinates are in units of $r/R_\star$.

obscured by the spiral arms. When viewed from the right, the arms present minimal absorption and both the X-ray emission and Hα emission are at maximum. When viewed from below, the denser, inner portion of the spiral pattern occults the X-ray source and both the Hα the X-ray emission are near a minimum. Finally, when viewed from the left, both once again return to a maximum.

This configuration agrees with typical LDI models, since the X-rays are distributed throughout the wind. However, in contrast to normal CIR models, the spiral patterns must have large column densities to account for the grey variability, and this implies that much of the wind flow is channeled through the CIRs.

Regardless of which, if either, configuration is correct, the important point is that cyclical X-ray variability is inconsistent with our current understanding of either wind structure formation, X-ray production, or both. Consequently, it may provide additional clues on how to interpret wind structure. Further, depending on how the wind material is distributed, the CIRs may account for a small fraction of the wind flow, as predicted by normal CIR theory (Lobel & Blomme 2008) or, if they originate from regions of localized magnetic activity (Cantiello & Braithwaite 2011), a much larger fraction. Thus, it is critical to verify our results if we are to arrive at a self-consistent understanding of stellar winds and mass loss rates in OB stars.

ACKNOWLEDGMENTS

We thank D. Huenemoerder and the CfA *Chandra* support staff for their assistance in understanding the data. We also thank the referee, Anthony Moffat, for comments that helped to clarify and enhance the contents of this paper. The scientific results reported in this article are based on observations made by the *Chandra* X-ray Observatory.

REFERENCES

Berghöefer, T. W., Baade, D., Schmitt, J. H. M. M., Kudritzki, R.-P., Puls, J., Hillier, D. J. & Pauldrach, A. W. A. 1996, A&A, 306, 899

Cantiello, M. & Braithwaite, J. 2011, A&A, 534A, 140
Cassinelli, J. P. 1983, ApJ, 268, 205
Chandra X-Ray Center 2012, Chandra Proposers Observatory Guide, Version 15.0, (Cambridge: CXC)
Chatfield, C. 2004, *The Analysis of Time Series, 6th ed*, (Washington, DC: Chapman & Hall/CRC), p.55
Cranmer, S. R., & Owocki, S. P. 1996, ApJ, 462, 469
de Jong, J. A., Henrichs, H. F., Kaper, L., Nichols, J. S., Bjorkman, K., Bohlender, D. A., Cao, H., Gordon, K., Hill, G., Jiang, Y., Kolka, I., Morrison, N., Neff, J., O'Neal, D., Scheers, B. & Telting, J. H. 2001, A&A, 368, 601
Eversberg, T., Lepine, S, & Moffat, A. F. J. 1998, ApJ, 494, 799
Feldmeier, A., Puls, J. & Pauldrach, A. W. A. 1997,A&A, 322, 878
Guedel, M. & Nazé, Y. 2009 A&ARv, 17, 309
Hamann, W.-R., Brown, J. C., Feldmeier, A. & Oskinova, L. M. 2001, A&A, 378, 946
Hillier, D. J. 1991, A&A, 247, 455
Hinkle, K., Wallace, L., Valenti, J., & Harmer, D. 2000, Visible and Near Infrared Atlas of the Arcturus Spectrum, 3727–9300 Å (San Francisco: Astronomical Society of the Pacific)
Howarth, I. D., Prinja, R. K. & Massa, D. 1995, ApJ, 452L, 65
Howarth, I. D., Bolton, C. T., Crowe, R. A., et al. 1993, ApJ, 417, 338
Huenemoerder, D. P., Mitschang, A., Dewey, D., Nowak, M. A., Schulz, N. S., et al. 2011, AJ, 141, 129
Ignace, R., Gayley, K. G., Hamann, W.-R., Huenemoerder, D. P., Oskinova, L. M., Pollock, A. M. T. & McFall, M. 2013, ApJ, in press, arXiv1307.7074
Kahn, S. M., Leutenegger, M. A., Cottam, J., et al. 2001, A&A, 365L, 312
Kaper, L., Henrichs, H. F., Nichols, J. S., Snoek, L. C., Volten, H. & Zwarthoed, G. A. A. 1996,A&As, 116, 257
Kaper, L., Henrichs, H. F., Nichols, J. S. & Telting, J. H. 1999,A&A, 344, 231
Lépine, S. & Moffat, A. F. J. 2008, AJ, 136, 548
Lobel, A. & Blomme. R. 2008, ApJ, 678, 408
Lucy. L. B. 1982, ApJ, 255, 286
Lucy, L. B. & White, R. L., 1980, ApJ, 24, 300
Markova, N., Puls, J., Scuderi, S. & Markov, H. 2005,A&A, 440, 1133
Massa, D., Fullerton, A. W., Nichols, J. S., Owocki, S. P., Prinja, R. K., St-Louis, N., Willis, A. J. et al. 1995, ApJ, 452, L53
Mullan, D. J. 1986, A&A, 165, 157
Nazé, Y., Oskinova, L. M. & Gosset, E. 2013, ApJ, 763, 143
Oskinova, L. M., Gayley, K. G., Hamann, W.-R., Huenemoerder, D. P., Ignace, R. & Pollock, A. M. T. 2012, ApJ, 747, 25
Oskinova, L.M., Clarke, D. & Pollock, A.M.T. 2001,A&A, 378, L21
Oskinova, L.M., Feldmeier, A. & Hamann, W.-R. 2004,A&A, 422, 675
Oskinova, L.M., Feldmeier, A., & Hamann, W.-R. 2006, MNRAS, 372, 313
Owocki, S. P., Castor, J. I. & Rybicki, G. B. 1988, ApJ, 335, 914
Owocki, S. P. 1999, in Proc. IAU Coll., 169, ed. B. Wolf, O. Stahl, & A. W. Fullerton, 294
Penny, L. R. 1996, ApJ, 463, 737
Preibisch, T. & Feigelson, E. D., 2005, ApJS, 160, 390
Prinja, R. K. & Massa, D. 2010,A&A, 521, L55
Vollmann, K., & Eversberg, T. 2006, Astronomische Nachrichten, 327, 862
Walborn, N. R. 1973, AJ, 78, 1067
Walborn, N. R., Nichols, J. S. & Waldron, W. L. 2009, ApJ, 703, 633
Walborn, N. R., Nichols-Bolin, J. & Panek, R. J. 1985, *International Ultraviolet Explorer Atlas of O-type Spectra from 1200 to 1900 Å*, (NASA Ref. Pub., 1155)